Communication

Single-Layer Dual-Band Linear-to-Circular Polarization Converter With Wide Axial Ratio Bandwidth and Different Polarization Modes

Hong Bin Wang and Yu Jian Cheng

Abstract—A dual-band linear-to-circular polarization converter (LCPC) based on a single-layer dielectric substrate is proposed. The element of the converter consists of two identical metallic layers with a combination of a connected Jerusalem cross (JC) and an "I"-type dipole for each layer. The proposed converter is designed by using an equivalent circuit model (ECM). Left-handed circularly polarized (LHCP) and right-handed circularly polarized (RHCP) beams can be, respectively, generated at *K*-band and *Ka*-band excited by a linearly polarized (LP) wave tilted 45° relative to the *x*- and *y*-directions of the converter. In addition, the converter covers two operation bands for *K*-/*Ka*-band satellite communications with high conversion efficiency and low polarization extinction ratio (PER). After full-wave optimization, the proposed converter is fabricated and measured. The measured results show a good agreement with the simulated ones. Even though there exists a tradeoff between the angular stability and the bandwidth of the dual-band LCPCs, the measured axial ratio (AR) remains stable in the lower operation band and a slight fluctuation in the higher band with the incident angle of 20°.

Index Terms—Dual band, high conversion efficiency, linear-to-circular polarization converter (LCPC), wide axial ratio (AR) bandwidth.

I. INTRODUCTION

Satellite communications become more and more important in future wireless applications [1]. A circularly polarized (CP) antenna is needed for the *K*-/*Ka*-band satellite communications. It should cover two operation bands, i.e., from 17.7 to 20.2 GHz and from 27 to 30 GHz. In addition, the polarization modes at two bands are orthogonal.

To achieve high aperture efficiency, shared-aperture antennas with multiple frequency bands and circular polarizations have been widely concerned in recent years [2]–[6]. However, most of the reported CP shared-aperture antennas are difficult to design at high frequency due to their complicated feeding networks. Consequently, researchers have paid more attention to linear-to-circular polarization converters (LCPCs) [7]–[17], which can generate CP waves combined with simple linearly polarized (LP) antennas [18]–[20] without the complicated feeding structures.

As we know, frequency-selective surfaces (FSSs) are widely used in the LCPC design. Generally, these LCPCs can be divided into two types, i.e., resonant FSS type [7]–[10] and nonresonant FSS type [11]–[14]. The resonant FSSs based on split slot rings [7], cross dipoles [8], modified cross slots [9], and Jerusalem cross (JC)

slots [10] are used to design LCPCs. These single resonant structures with large element spacing perform high insertion loss and narrow axial ratio (AR) bandwidth. Other than those resonant structures, the nonresonant structures based on subwavelength elements show wideband capability and remain stable for large angle incidence. The structure presented in [12] is based on the conventional meander lines and loops to improve 3 dB AR bandwidth up to 46.8% with the incident angle of 30°. However, it performs 3 dB insertion loss by using a single layer. To improve the AR bandwidth and reduce the insertion loss, multilayer meander lines [13], [14] and FSSs [15]–[17] are used. In addition, the single-band LCPCs in [13] and [17] show the stable responses for the 45° oblique incidence.

Except for the aforementioned single-band LCPCs, dual-band LCPCs have been increasingly concerned for dual-band and compact communication systems. Compared to the single-band LCPCs, the dual-band LCPCs generally show low angular stabilities and narrow operation bands due to the mutual coupling between the two frequency band structures. Some dual-band LCPCs [21], [22] in reflection modes are generally used as reflectors, which cause feed blockages in the applications. Several dual-band transmission-type LCPCs based on single- [23] and two-layered [24], [25] structures are reported. However, these dual-band LCPCs with similarly split-loop structures perform either strong couplings between two orthogonal components or strong mutual interferences between dual-band structures. They usually perform high insertion loss. The dual-band LCPC presented in [26] and [27] is based on antenna–filter–antenna elements with three metallic layers. It is operated at 20/30 GHz with low insertion losses but narrow bandwidths. Hosseini and Hum [28] design a dual-band LCPC by using a systematic circuit-driven methodology. The polarization converter based on five-layered modified JC offers low insertion losses of 0.6 dB and 4%/2.7% AR bandwidths at 20/30 GHz, respectively. It should be noted that the five-layered structure is relatively bulky and leads to fabrication error due to misalignment between each layer. In addition, the converter performs the same circular polarization in the dual band. Relatively, the dual-band and dual-CP LCPC is difficult to design.

In this communication, a dual-band and dual-CP LCPC based on a combination of the connected JCs and "I"-type dipoles is presented by using a single substrate with two identical metallic layers, as shown in Fig. 1. The combination of the JCs and "I"-type dipoles can achieve the dual-band response. To be specific, the combined structure in the single layer offers multiple equivalent lumped elements instead of two [29] or less [17] lumped elements. This feature provides more freedom for the operation band and bandwidth control by using less number of layers, which makes the converter low profile and easy for fabrication compared to multilayer structures for the dual-band design. The left-handed CP (LHCP) wave in the lower band and the right-handed CP (RHCP) wave in the higher band can be achieved by simply adjusting the dimensions of the converter.

This communication is organized as follows. Section II provides the selection of the converter element and the equivalent circuit
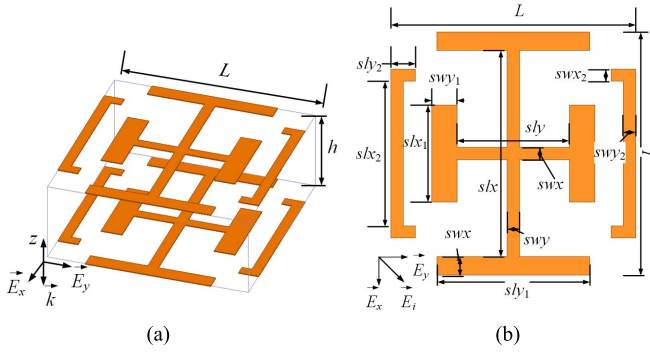
Fig. 1. Configuration of the proposed LCPC element. (a) 3-D view. (b) Top view. $L = 4$, $slx = 3.4$, $slx_1 = 1.6$, $slx_2 = 2.38$, $sly = 1.83$, $sly_1 = 2.5$, $sly_2 = 0.4$, $swx = 0.2$, $swx_1 = 0.3$, $swx_2 = 0.2$, $swy = 0.21$, $swy_1 = 0.42$, and $swy_2 = 0.2$ (unit: millimeters).

model (ECM) for the converter. In Section III, the dual-band converter is optimized by using the ECM and fine-tuned by HFSS. Then, several simulated results for the final structure are given. After that, the sample converter is fabricated and measured in Section IV. The measured results for different incident angles are discussed. Meanwhile, the performances of some single-/dual-band LCPCs are compared with each other in Section IV. Finally, Section V provides the conclusion.

II. PRINCIPLE OF OPERATION

A. Selection of Converter Element

In the past several years, there have been many kinds of elements applied to the CP generation. The main structures can be classified into four types, i.e., the center connected dipole, the rectangular patch, the rectangular loop, and the combination type. As we know, the center connected type can be suitable for CP generation [29]–[31]. For example, the cross dipole shows high polarization isolation between two orthogonal arms, which allows the independent adjustment of the vertical and horizontal components. Obviously, this structure reduces the complexity of the CP device design. However, the periodic arrangements of the cross dipoles usually lead to a large unit length. Different from the cross dipoles, the elements based on the rectangular patches or loops show a denser lattice. Unfortunately, the mutual coupling between the two orthogonal components is strong, increasing the design difficulty. As the center connected structure, the JC structure not only possesses the advantages of the cross dipole but also shows more freedom in design and smaller element spacing than the cross dipole due to four caps on the ends. Finally, the combination of the JC structure and "I"-type dipole is selected in this communication, as shown in Fig. 1. The horizontal arm of the JC structure and the vertical "I"-type dipole offers lower and higher frequency resonances, which control both the transmission responses. Thanks to the connected arm of the JC structure in the vertical direction, it offers the inductance to optimize the transmission responses in both operation bands.

B. Equivalent Circuit Model

Considering an incident LP wave is traveling along the $-z$-direction, with the electric field vector $\vec{E}^i$, tilted 45° relative to both x- and y-directions. The incident electric field can be decomposed into two components, $\vec{E}_x^i$ (x-direction) and $\vec{E}_y^i$ (y-direction), with the same magnitude and phase

$$\vec{E}^i = 1/\sqrt{2}\left(\vec{E}_x^i + \vec{E}_y^i\right) = 1/\sqrt{2}E^i(\vec{e}_x + \vec{e}_y)e^{jkz} \qquad (1)$$
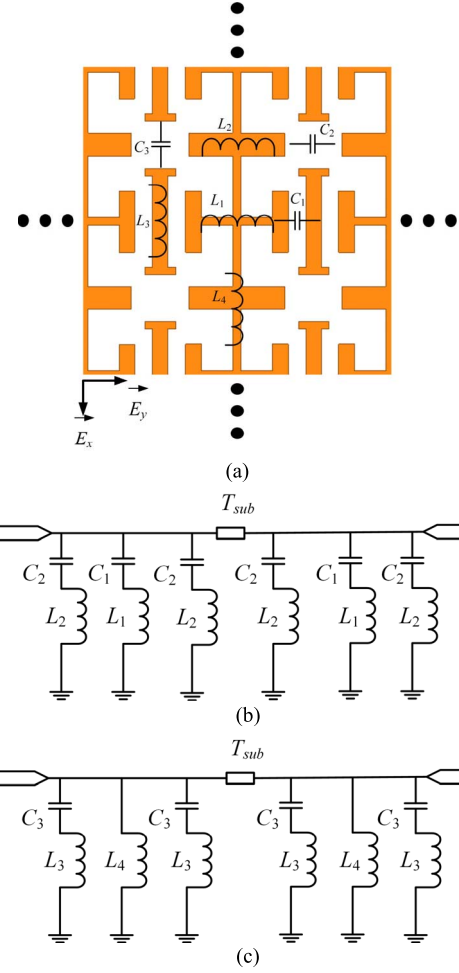

Fig. 2. ECMs of the proposed converter. (a) Representations of circuit parameters. (b) y-direction. (c) x-direction. $C_1 = 10$ fF, $C_2 = 4.1$ fF, $C_3 = 5.1$ fF, $L_1 = 4.7$ nH, $L_2 = 1.2$ nH, $L_3 = 4.4$ nH, and $L_4 = 2$ nH.

where $\vec{e}_x$ and $\vec{e}_y$ are the unit vectors in the x- and y-directions, respectively. Then, the transmitted E-field can be calculated as

$$\begin{pmatrix} E_x^t \\ E_y^t \end{pmatrix} = 1/\sqrt{2} \begin{pmatrix} T_{xx} & T_{xy} \\ T_{yx} & T_{yy} \end{pmatrix} \begin{pmatrix} E^i \\ E^i \end{pmatrix} \qquad (2)$$

where

$$T_{xx} = |T_{xx}|e^{j\varphi_{xx}} \text{ and } T_{yy} = |T_{yy}|e^{j\varphi_{yy}}$$

represent the copolarization transmission coefficients, respectively. As the center connected structure, the proposed structure has weak mutual coupling between the two orthogonal components, which can be negligible [30], [31]. Thus, the magnitudes of the cross-polarization transmission coefficients T_{xy} and T_{yx} can be negligible.

Since T_{xy} and T_{yx} are negligible, the ECMs of the proposed LCPC can be separated for the x- and y-directions, as shown in Fig. 2. For simplicity, the two metallic layers on the top and bottom sides of the substrate are identical. Thus, the ECMs are symmetric. It is worth noting that the two layers yield sufficient isolation when the element length, L, and the substrate thickness, h, satisfy $L/h = 1.3$–3 according to [32]. In the models, inductances L_1, L_2, and L_4 are caused by the modified JC structure, whereas L_3 denotes the "I"-type dipole in the x-direction. Capacitances C_1, C_2, and C_3 represent the effect of the fringing field in the vertical and horizontal gaps. T_{sub} denotes the transmission line substitute for the substrate.

According to (2), the transmission coefficients T_{xx} and T_{yy} can denote the polarization of the output electromagnetic wave substituted

for the transmitted electric fields. If the magnitudes and phases of the transmission coefficients satisfy the condition as follows:

$$|T_{xx}| = |T_{yy}|, \quad \Delta\varphi = \varphi_{yy} - \varphi_{xx} = \pm 90° \qquad (3)$$

the CP wave can be generated. In terms of the proposed converter, the transmitted wave is RHCP when $\varphi = 90°$ and LHCP when $\varphi = -90°$.

III. DUAL-BAND LCPC DESIGN

The motivation of this communication is to design an LCPC covering the operation frequency band from 17.7 to 20.2 GHz and from 27 to 30 GHz for K-/Ka-band satellite communications. As mentioned in Section II, the copolarization transmission coefficients with the same magnitude and 90° phase difference can generate the CP wave. In order to characterize the CP wave in an intuitive way, the AR is used to reflect the degree of the CP. This parameter can be calculated in the following equation:

$$AR = \sqrt{\frac{\left(T_{xx}^2 + T_{yy}^2 + \sqrt{T_{xx}^4 + T_{yy}^4 + 2T_{xx}^2 T_{yy}^2 \cos(2\Delta\varphi)}\right)}{\left(T_{xx}^2 + T_{yy}^2 - \sqrt{T_{xx}^4 + T_{yy}^4 + 2T_{xx}^2 T_{yy}^2 \cos(2\Delta\varphi)}\right)}}. \quad (4)$$

When AR = 1, the transmitted wave is a CP wave. When AR = ∞, the transmitted wave is an LP wave. In other cases, the transmitted wave is an elliptically CP wave. In this communication, the used dielectric substrate is TLY-5 with the relative dielectric permittivity $\varepsilon_r = 2.2$ and the thickness $h = 1.575$ mm.

According to the ECMs shown in Fig. 2, the impedances of each metallic layer for the x- and y-directions, Z_x and Z_y, respectively, are calculated as follows:

$$Z_y = \frac{(1 - \omega^2 L_1 C_1)(1 - \omega^2 L_2 C_2)}{j\omega(C_1 + 2C_2 - 2\omega^2 L_1 C_1 C_2 - \omega^2 L_2 C_1 C_2)} \qquad (5)$$

$$Z_x = \frac{j\omega L_4(1 - \omega^2 L_3 C_3)}{1 - \omega^2 C_3(L_3 + 2L_4)}. \qquad (6)$$

Considering the ECM is symmetric, the ABCD matrix for the y-direction can be obtained subsequently in the following equation [33]:

$$\begin{bmatrix} A & B \\ C & D \end{bmatrix}_y$$
$$= \begin{bmatrix} \cos\theta_d + j\dfrac{Z_d}{Z_y}\sin\theta_d & jZ_d\sin\theta_d \\ \dfrac{2\cos\theta_d}{Z_y} + j\left(\dfrac{1}{Z_d} + \dfrac{Z_d}{Z_y^2}\right)\sin\theta_d & \cos\theta_d + j\dfrac{Z_d}{Z_y}\sin\theta_d \end{bmatrix} \qquad (7)$$

where Z_d denotes the impedance of the substrate and θ_d stands for the phase shift of the incident wave transmitting through the substrate, respectively. According to the relationship between the ABCD matrix and S-parameters, T_{yy} can be calculated in the following equation:

$$T_{yy} = \frac{2}{A + B/Z_0 + CZ_0 + D} \qquad (8)$$

where Z_0 is the free-space impedance. Similarly, T_{xx} can be calculated as well.

Based on the formulas mentioned above, ECMs can be optimized in the Keysight Advanced Design System (ADS), to satisfy the objective of the 3 dB AR bandwidths of 13%/11% in the K-/Ka-band. Genetic and gradient algorithms are adopted in the optimization process. The final values of the circuit parameters are listed in Fig. 2. Then, the initial dimensions of the converter according to the circuit parameters can be obtained referring to [34] as follows:

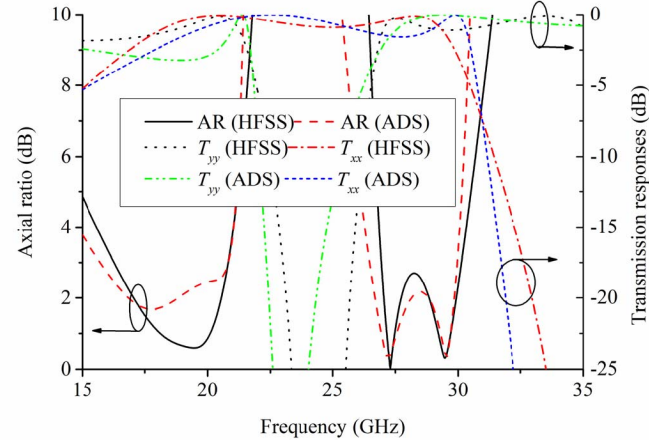$$L_i = \frac{\mu_0 L}{2\pi} \ln\left(\left(\sin\frac{\pi m}{2L}\right)^{-1}\right), \quad i = 1, 2, 3, 4 \qquad (9)$$

Fig. 3. Simulated transmission responses and AR of the proposed converter.

$$C_j = \frac{2\varepsilon_0 \varepsilon_{eff} L}{\pi} \ln\left(\left(\sin\frac{\pi n}{2L}\right)^{-1}\right), \quad j = 1, 2, 3 \qquad (10)$$

where μ_0 and ε_0 are the permeability and permittivity in vacuum and $\varepsilon_{eff} = \sqrt{(\varepsilon_r + 1)/2}$ is the equivalent permittivity of the substrate. In (9), $m = swx, swx_1, swy_2$, and swy in order when i is ranged from 1 to 4. In (10), n equals to $(L - sly)/2 - swy_2 - swy_1$, $L - sly_1$, and $L - slx_2 - 2swx_2$ in order when j is ranged from 1 to 3. Finally, the structural parameters can be fine-tuned by using the commercial software HFSS. The final parameters of the converter are listed in Fig. 1. The transmission coefficients and ARs obtained by ADS and HFSS are shown in Fig. 3. It is worth noting that the HFSS results include the couplings among the orthogonal arms of the JC structure and the "I"-type dipole in each layer. However, the mutual effects among the orthogonal arms of the JC structure and the "I"-type dipole are not considered in the ECMs for simplicity, which makes the ADS results slightly different from the HFSS results. Even so, the results show a good agreement with each other.

To be specific, the magnitudes of the transmission coefficients remain over −1.5 dB in the range of 17.72–21.37 and 26.94–29.53 GHz. In the lower band, the "I"-type dipole performs capacitive, which leads to the phase of T_{xx} ahead of that of T_{yy} caused by the horizontal arm of the JC structure. As the frequency increases and remains below the resonant frequency of the "I"-type dipole, the phase of T_{yy} increases rapidly and gets ahead of the phase of T_{xx} due to the horizontal arm resonance. As a result, the transmitted field is LHCP with the 3 dB AR bandwidth of 24% from 16.28 to 20.82 GHz, whereas the transmitted field becomes RHCP with the 3 dB AR bandwidth of 11% from 26.94 to 30.13 GHz. Fig. 4 shows the current distribution on the output surface for $t = 0$, $T/4$, $T/2$, and $3T/4$ at 18.55 GHz. The orientation of the current corresponds to the scattering of the E-field, which rotates by 90° with a quarter period. It can be seen that the surface current is concentrated on the JC surface with the clockwise rotation and nearly the same intensity, which is demonstrated to generate the LHCP wave. On the contrary, the surface current at 28.54 GHz as shown in Fig. 5 is caused alternately by the JC structure and the "I"-type dipole at different times with the anticlockwise rotation, which leads to the RHCP wave.

Another parameter to characterize the CP wave is the linear-to-circular transmission coefficient [25], as shown in Fig. 6. The magnitude of the LHCP transmission coefficient remains over −1 dB from 18.46 to 21.27 GHz. Meanwhile, the magnitude of the RHCP trans-
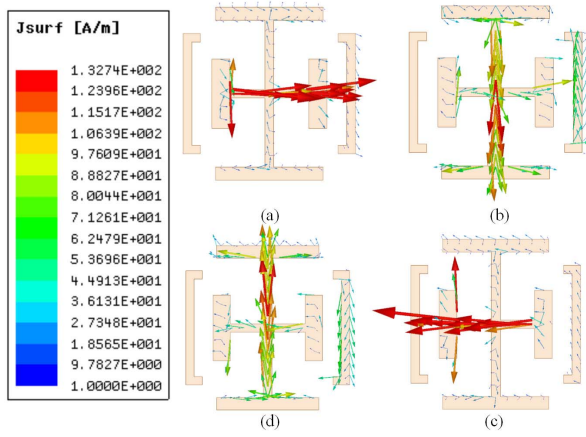
Fig. 4. Surface current distribution of the proposed converter at 18.55 GHz. (a) $t = 0$. (b) $t = T/4$. (c) $t = T/2$. (d) $t = 3T/4$.
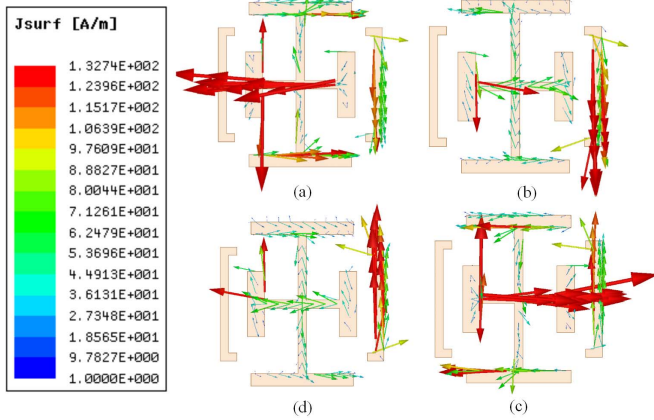

Fig. 5. Surface current distribution of the proposed converter at 28.54 GHz. (a) $t = 0$. (b) $t = T/4$. (c) $t = T/2$. (d) $t = 3T/4$.
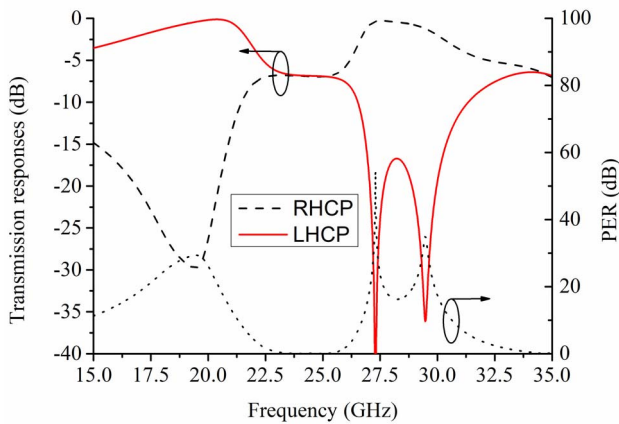

Fig. 6. Linear-to-circular transmission coefficients and PERs of the proposed converter.

mission coefficient remains over -1 dB from 26.97 to 29.27 GHz. In addition, the polarization extinction ratios (PERs) [24], defined as the difference between the co-CP and cross-CP transmission coefficients, are high in both the operation bands. They are 27.87 dB at 18.55 GHz and 17.39 dB at 28.54 GHz. The minimum PER is nearly 16 dB in both the operation bands.

To make the proposed converter understood clear, the main parameters, sly, sly_1, and slx_2, are studied. The transmission zeros of T_{yy} caused by the horizontal arm of the JC move down with the increase
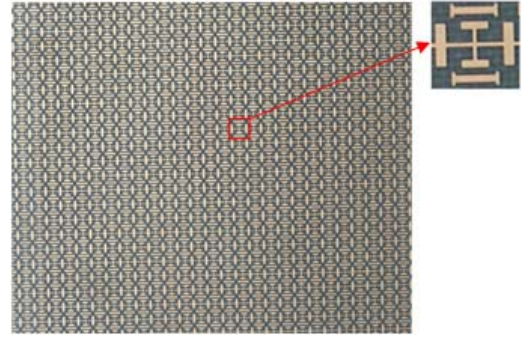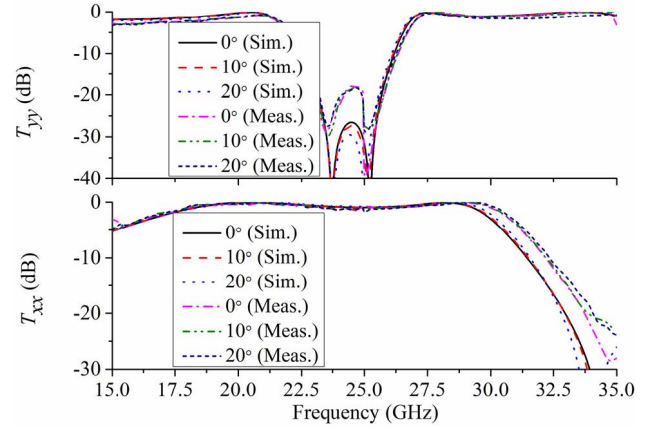

Fig. 7. Photograph of the fabricated LCPC sample.

Fig. 8. Simulated and measured transmission responses of the proposed converter at different incident angles.

of sly, while T_{xx} remains stable. Similarly, the transmission zero of T_{xx} shifts down with the increase of the length of the "I"-type dipole. Meanwhile, T_{yy} is stable.

IV. EXPERIMENTAL RESULTS

The proposed LCPC based on the single substrate is fabricated by using a normal PCB process. The photograph of the fabricated sample is shown in Fig. 7, which consists of 70×70 elements with the total size of 280×280 mm^2. Two horn antennas connected to the vector network analyzer (VNA) with the coaxial cables are placed at two sides of the converter. They act as transmitting and receiving antennas, respectively. The converter in the middle is fixed on the rotary platform with the rotation of $45°$ relative to the x-direction of the converter. The receiving antenna is also rotated to $\pm 45°$ around the horizontal axis for different polarizations.

The measured transmission responses for both the x-direction and y-direction polarizations at oblique incidence are compared to the simulated results shown in Fig. 8. It can be seen that the measured results have a good agreement with the simulated ones. The measured magnitude of T_{xx} remains stable and that of T_{yy} shows a slight fluctuation, especially in the higher band as the incident angle increases. Also, the phase differences between both the transmission responses are simulated and measured which are not shown here for brevity. Similarly, the measured phase difference performs nearly unchanged in the lower band but decreases slightly in the higher band with the increasing incident angle as well as the simulated one. As shown in Fig. 9, the bandwidth of the measured AR is a little wider than that of the simulated AR due to a slight shift of the measured transmission responses compared to the simulated ones. The AR remains stable in the lower band and a little deteriorated in the higher band as the incident angle increases. It is because the

TABLE I
PERFORMANCE COMPARISONS AMONG SINGLE-/DUAL-BAND LCPCS

|	Center frequency (GHz)	Insertion loss (dB)	AR Bandwidth	Thickness	Cell size	Metallic layers	Polarization modes at different bands	Angular stability
[12]	23.5	3	46.8%	$0.02\lambda_1$	$0.27\lambda_1$	1	-	30°
[15]	8.48	<2	64%	$0.17\lambda_1$	$0.42\lambda_1$	4	-	20°
[17]	10	2.78	40%	$0.18\lambda_1$	$0.15\lambda_1$	7	-	45°
[24]	9.77, 11.84	1.6, 4	-	$0.03\lambda_1$	$0.21\lambda_1$	2	Orth.	-
[25]	5.1, 6.4	6, 5	-	$0.02\lambda_1$	$0.26\lambda_1$	2	Orth.	-
[27]	19.95, 29.75	<1, <2	2.5%, 1.7%	$0.07\lambda_1$	$0.35\lambda_1$	3	Orth.	30°
[28]	19.6, 29.6	0.6, 0.6	4%, 2.7%	$0.31\lambda_1$	-	5	Same	-
This work	18.5, 29	2, 0.8	29%, 12%	$0.10\lambda_1$	$0.25\lambda_1$	2	Orth.	20°
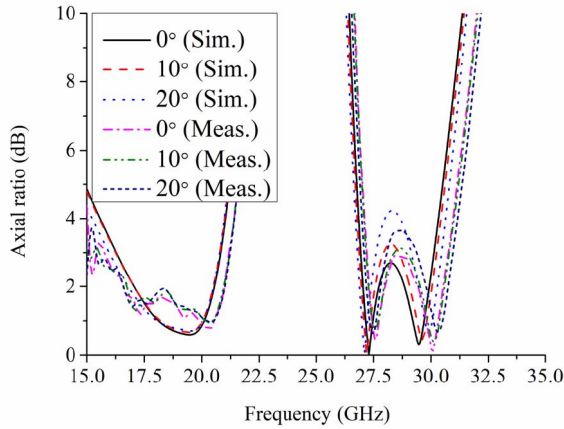
Fig. 9. Simulated and measured ARs of the proposed converter at different incident angles.

response in the lower band is caused by the connected JCs which are more insensitive to the incident angle due to their nonresonant structures. Conversely, the higher passband response, influenced by the mutual coupling between the JCs and the "I"-type dipoles which are resonant structures, is slightly affected by the oblique incidence.

There are some performance comparisons among the single-/dual-band LCPCs as listed in Table I. It can be seen that the single-band LCPCs generally perform wideband response with the oblique angle up to 45°. Compared to the single-band LCPCs, the dual-band LCPCs show low angular stabilities and narrow operation bands. The proposed converter shows the broadband performances with the single substrate in both the operation bands in spite of low angular stability. In addition, this structure shows a good tradeoff between the insertion loss and the number of the metallic layers.

V. CONCLUSION

This communication presents a K-/Ka-band LCPC based on a single substrate. The converter consists of the single substrate and two identical metallic layers with a combination of connected JCs and "I"-type dipoles for each layer. An ECM is used to optimize the converter, and then the physical dimensions are fine-tuned by HFSS. The output wave becomes LHCP in the K-band and RHCP in the Ka-band when transmitted through the converter. Then, the proposed converter is fabricated and measured. The measured results show a good agreement with the simulated ones. The measured AR bandwidths reach 29% and 12% in the lower and higher bands, respectively, which cover the operation bandwidths of K-/Ka-band satellite communication. Different from the single-band LCPCs, there exists a tradeoff between the angular stability and the bandwidth of the dual-band LCPCs. Even so, the measured AR remains stable

in the lower operation band and a slight fluctuation in the higher band with the incident angle of 20°. Compared to other dual-band converters, this structure shows the broadband performances in both the operation bands with less number of the metallic layers.

REFERENCES

[1] E. Lutz, D. Cygan, M. Dippold, F. Dolainsky, and W. Papke, "The land mobile satellite communication channel-recording, statistics, and channel model," *IEEE Trans. Vehic. Technol.*, vol. 40, no. 2, pp. 375–386, May 1991.

[2] Y. Ushijima, E. Nishiyama, and M. Aikawa, "Single-layer integrated microstrip array antenna for dual circular polarisation," *IET Microw. Antennas Propag.*, vol. 6, no. 8, pp. 962–968, Jun. 2012.

[3] J.-D. Zhang, W. Wu, and D-G. Fang, "Dual-band and dual-circularly polarized shared-aperture array antennas with single-layer substrate," *IEEE Trans. Antennas Propag.*, vol. 64, no. 1, pp. 109–116, Jan. 2016.

[4] C.-X. Mao, S. Gao, Y. Wang, Q.-X. Chu, and X.-X. Yang, "Dual-band circularly polarized shared-aperture array for C -/ X-band satellite communications," *IEEE Trans. Antennas Propag.*, vol. 65, no. 10, pp. 5171–5178, Oct. 2017.

[5] Y. J. Cheng, J. Wang, and X. L. Liu, "94 GHz substrate integrated waveguide dual-circular-polarization shared-aperture parallel-plate long-slot array antenna with low sidelobe level," *IEEE Trans. Antennas Propag.*, vol. 65, no. 11, pp. 5855–5861, Nov. 2017.

[6] J. F. Zhang, Y. J. Cheng, Y. R. Ding, and C. X. Bai, "A dual-band shared-aperture antenna with large frequency ratio, high aperture reuse efficiency, and high channel isolation," *IEEE Trans. Antennas Propag.*, vol. 67, no. 2, pp. 853–860, Feb. 2019.

[7] M. Euler, V. Fusco, R. Cahill, and R. Dickie, "325 GHz single layer sub-millimeter wave FSS based split slot ring linear to circular polarization convertor," *IEEE Trans. Antennas Propag.*, vol. 58, no. 7, pp. 2457–2459, Aug. 2010.

[8] G. I. Kiani and V. Dyadyuk, "Quarter-wave plate polariser based on frequency selective surface," in *Proc. 40th Eur. Microw. Conf.*, Sep. 2010, pp. 1361–1364.

[9] H. B. Wang and Y. J. Cheng, "140 GHz linear to circular polarization convertor based on modified cross slot frequency selective surface with high selectivity," in *Proc. 12th Eur. Conf. Antennas Propag. (EuCAP)*, Apr. 2018, pp. 1–4.

[10] I. Sohail, Y. Ranga, K. P. Esselle, and S. G. Hay, "A linear to circular polarization converter based on Jerusalem-cross frequency selective surface," in *Proc. 7th Eur. Conf. Antennas Propag. (EuCAP)*, Apr. 2013, pp. 2141–2143.

[11] L. Young, L. Robinson, and C. Hacking, "Meander-line polarizer," *IEEE Trans. Antennas Propag.*, vol. AP-21, no. 3, pp. 376–378, May 1973.

[12] P. Fei, Z. Shen, X. Wen, and F. Nian, "A single-layer circular polarizer based on hybrid meander line and loop configuration," *IEEE Trans. Antennas Propag.*, vol. 63, no. 10, pp. 4609–4614, Oct. 2015.

[13] M.-A. Joyal and J.-J. Laurin, "Analysis and design of thin circular polarizers based on meander lines," *IEEE Trans. Antennas Propag.*, vol. 60, no. 6, pp. 3007–3011, Jun. 2012.

[14] F. F. Manzillo, M. Ettorre, R. Sauleau, and A. Grbic, "Systematic design of a class of wideband circular polarizers using dispersion engineering," in *Proc. 11th Eur. Conf. Antennas Propag. (EuCAP)*, Mar. 2017, pp. 1279–1281.

[15] W. Zhang, J.-Y. Li, and J. Xie, "A broadband circular polarizer based on cross-shaped composite frequency selective surfaces," *IEEE Trans. Antennas Propag.*, vol. 65, no. 10, pp. 5623–5627, Oct. 2017.

[16] L. Martinez-Lopez, J. Rodriguez-Cuevas, J. I. Martinez-Lopezand, and A. E. Martynyuk, "A multilayer circular polarizer based on bisected split-ring frequency selective surfaces," *IEEE Antennas Wireless Propag. Lett.*, vol. 13, pp. 153–156, Jan. 2014.

[17] S. M. A. M. H. Abadi and N. Behdad, "Wideband linear-to-circular polarization converters based on miniaturized-element frequency selective surfaces," *IEEE Trans. Antennas Propag.*, vol. 64, no. 2, pp. 525–534, Feb. 2016.

[18] Y. F. Wu, Y. J. Cheng, and Z. X. Huang, "Ka-band near-field-focused 2-D steering antenna array with a focused rotman lens," *IEEE Trans. Antennas Propag.*, vol. 66, no. 10, pp. 5204–5213, Oct. 2018.

[19] Y. J. Cheng, W. Hong, and K. Wu, "94 GHz substrate integrated monopulse antenna array," *IEEE Trans. Antennas Propag.*, vol. 60, no. 1, pp. 121–129, Jan. 2012.

[20] J. Wu, Y. J. Cheng, and Y. Fan, "A wideband high-gain high-efficiency hybrid integrated plate array antenna for v-band inter-satellite links," *IEEE Trans. Antennas Propag.*, vol. 63, no. 4, pp. 1225–1233, Apr. 2015.

[21] N. J. G. Fonseca and C. Mangenot, "High-performance electrically thin dual-band polarizing reflective surface for broadband satellite applications," *IEEE Trans. Antennas Propag.*, vol. 64, no. 2, pp. 640–649, Feb. 2016.

[22] W. Tang, S. Mercader-Pellicer, G. Goussetis, H. Legay, and N. J. G. Fonseca, "Low-profile compact dual-band unit cell for polarizing surfaces operating in orthogonal polarizations," *IEEE Trans. Antennas Propag.*, vol. 65, no. 3, pp. 1472–1477, Mar. 2017.

[23] Y. Ranga, L. Matekovits, S. G. Hay, and T. S. Bird, "An anisotropic impedance surface for dual-band linear-to-circular transmission polarization convertor," in *Proc. Int. Workshop Antenna Technol. (iWAT)*, Karlsruhe, Germany, Mar. 2013, pp. 47–50.

[24] H.-X. Xu, G.-M. Wang, M. Q. Qi, T. Cai, and T. J. Cui, "Compact dual-band circular polarizer using twisted Hilbert-shaped chiral metamaterial," *Opt. Express*, vol. 21, no. 21, 2013, Art. no. 24912.

[25] M. Mutlu, A. E. Akosman, A. E. Serebryannikov, and E. Ozbay, "Asymmetric chiral metamaterial circular polarizer based on four U-shaped split ring resonators," *Opt. Lett.*, vol. 36, no. 9, pp. 1653–1655, May 2011.

[26] P. Naseri, C. A. Fernandes, S. A. Matos, and J. R. Costa, "Antenna-filter-antenna-based cell for linear-to-circular polarizer transmit-array," in *Proc. IEEE Int. Symp. Antennas Propag. & USNC/URSI Nat. Radio Sci. Meeting* Jul. 2017, pp. 1071–1072.

[27] P. Naseri, S. A. Matos, J. R. Costa, C. A. Fernandes, and N. J. G. Fonseca, "Dual-band dual-linear-to-circular polarization converter in transmission mode application to k/ka-band satellite communications," *IEEE Trans. Antennas Propag.*, vol. 66, no. 12, pp. 7128–7137, Dec. 2018.

[28] M. Hosseini and S. V. Hum, "A systematic circuit-based approach to efficiently realize single- and dual-band circular polarizers," in *Proc. 12th Eur. Conf. Antennas Propag. (EuCAP)*, Apr. 2018, pp. 1–5.

[29] M. Hosseini and S. V. Hum, "A circuit-driven design methodology for a circular polarizer based on modified Jerusalem cross grids," *IEEE Trans. Antennas Propag.*, vol. 65, no. 10, pp. 5322–5331, Oct. 2017.

[30] G.-B. Wu, S.-W. Qu, S. Yang, and C. H. Chan, "Broadband, single-layer dual circularly polarized reflectarrays with linearly polarized feed," *IEEE Trans. Antennas Propag.*, vol. 64, no. 10, pp. 4235–4241, Oct. 2016.

[31] R. Chaharmir, J. Shaker, and M. Cuhaci, "Development of dual-band circularly polarised reflectarray," *Proc. Inst. Elect. Eng.–Microw., Antenna Propag.*, vol. 153., no. 1, pp. 49–54, Feb. 2006.

[32] M. Hosseini and M. Hakkak, "Characteristics estimation for Jerusalem cross-based artificial magnetic conductors," *IEEE Antennas Wireless Propag. Lett.*, vol. 7, pp. 58–61, Apr. 2008.

[33] D. M. Pozar, *Microwave Engineering*. 3rd ed. New York, NY, USA: Wiley, 2005, ch. 4.

[34] O. Luukkonen *et al.*, "Simple and accurate analytical model of planar grids and high-impedance surfaces comprising metal strips or patches," *IEEE Trans. Antennas Propag.*, vol. 56, no. 6, pp. 1624–1632, Jun. 2008.